Research Article

Development of Dry Powder Inhaler Patient Interfaces for Improved Aerosol Delivery to Children

Karl Bass[1] and Worth Longest[1,2,3]

Abstract. The objective of this study was to explore different internal flow passages in the patient interface region of a new air-jet–based dry powder inhaler (DPI) in order to minimize device and extrathoracic aerosol depositional losses using computational fluid dynamics (CFD) simulations. The best-performing flow passages were used for oral and nose-to-lung (N2L) aerosol delivery in pediatric extrathoracic airway geometries consistent with a 5-year-old child. Aerosol delivery conditions were based on a previously developed and tested air-jet DPI device and included a base flow rate of 13.3 LPM (delivered from a small ventilation bag) and an inhaled air volume of 750 mL. Initial CFD models of the system clearly established that deposition on either the back of the throat or nasal cannula bifurcation was strongly correlated with the maximum velocity exiting the flow passage. Of all designs tested, the combination of a 3D rod array and rapid expansion of the flow passage side walls was found to dramatically reduce interface and device deposition and improve lung delivery of the aerosol. For oral aerosol administration, the optimal flow passage compared with a base case reduced device, mouthpiece, and mouth-throat deposition efficiencies by factors of 8-, 3-, and 2-fold, respectively. For N2L aerosol administration, the optimal flow pathway compared with a base case reduced device, nasal cannula, and nose-throat deposition by 16-, 6-, and 1.3-fold, respectively. In conclusion, a new patient interface design including a 3D rod array and rapid expansion dramatically improved transmission efficiency of a dry powder aerosol.

KEY WORDS: air-jet dry powder inhaler (DPI); turbulent jet; jet attenuation; 3D rod array; patient interfaces.

INTRODUCTION

Delivery of pharmaceutical aerosols to the lungs typically requires a nebulizer, metered dose inhaler (MDI), or dry powder inhaler (DPI). For the treatment of lung infections in pediatric patients with cystic fibrosis (CF), tobramycin inhaled powder *via* a DPI can be administered to potentially eradicate bacterial colonies. DPIs provide several advantages, compared with using tobramycin inhaled solution in a nebulizer, as higher doses of the antibiotic can be delivered faster and the devices are easier to load and clean (1). However, DPIs are associated with several disadvantages including poor lung delivery efficiencies, especially in children, as well as requiring inhalation maneuvers that may be difficult for children to achieve. For DPI use in children with oral inhalation, Below et al. (2) reported 5% and 22% of nominal dose

was deposited on a tracheal filter in *in vitro* experiments when testing the Novolizer and Easyhaler, respectively. Similarly, Lindert et al. (3) reported 9 to 11% lung delivery efficiency when testing the Cyclohaler, HandiHaler, and Spinhaler with pediatric *in vitro* conditions. These devices were developed for use by adults, not the pediatric patients that are the focus of this study, and the poor delivery performance may be attributed to insufficient inhalation flow rates to correctly empty the inhaler and deaggregate the powder. Inhalation flow rate and other device design considerations were considered in two studies by Lexmond et al. (4,5), who concluded that it is of paramount importance to design devices specifically for children when developing DPIs and pediatric delivery systems.

Our group has recently published several studies related to the ongoing development of a pediatric DPI for the delivery of tobramycin, as a spray-dried excipient enhanced growth (EEG) formulation, to children with CF (6–9). The full delivery system includes a ventilation bag, inline air-jet DPI, and patient interface, which is described in detail by Farkas et al. (6), and is designed to be as compact and portable as possible. The ventilation bag provides a positive pressure gas source to actuate the device with approximately 750 mL of air for a 5-year-old child, which allows for oral or

[1] Department of Mechanical and Nuclear Engineering, Virginia Commonwealth University, 401 West Main Street, P.O. Box 843015, Richmond, Virginia 23284-3015, USA.

[2] Department of Pharmaceutics, Virginia Commonwealth University, Richmond, Virginia, USA.

[3] To whom correspondence should be addressed. (e–mail: pwlongest@vcu.edu)

nasal administration and inhibits exhalation by the patient in the reverse direction through the device. The air-jet DPI is composed of small diameter inlet and outlet capillaries that penetrate a capsule-shaped powder chamber. The inlet capillary provides a high-velocity, compressible, and turbulent air-jet to the chamber that aerosolizes the powder and delivers the aerosol to the patient interface *via* the outlet capillary. Bass et al. (9) presented an optimized inlet and outlet capillary configuration that maximized aerosolization performance in terms of high emitted dose (ED) and low particle size, which was quantified by the mass-median aerodynamic diameter (MMAD) of the aerosol.

The present study builds upon the experimental work by Farkas et al. (6), which presented an evaluation of losses in the mouthpiece (MP) and mouth-throat (MT) for oral administration and nasal cannula (NC) and nose-throat (NT) for nasal administration. The Farkas et al. study (6) actuated the high-efficiency pediatric air-jet DPI with an inhalation volume for 750 mL, for a 5–6-year-old subject, and with a 6 kPa pressure drop, which is consistent with hand actuation of a small ventilation bag. The device was loaded with 10 mg of EEG albuterol sulfate (AS) as a surrogate test formulation (in place of tobramycin powder) and was actuated in connection with either *in vitro* 5-year-old MT or NT models to test MP or NC patient interfaces, respectively. The best-case DPI and MP combination for oral administration resulted in 21.8% device loss, 4.6% interface loss, and 6.6% MT loss, which produced an estimated lung dose of 63.8% on the tracheal filter (96.8% recovery). The best-case DPI and NC combination for nose-to-lung (N2L) delivery resulted in 21.9% device loss, 6.1% interface loss, and 8.3% NT loss, which resulted in an estimated lung dose of 60.7% on the tracheal filter (97.1% recovery). In an effort to maximize estimated lung dose, the current study aims to develop the MP and NC further to reduce interface and extrathoracic (ET) losses for oral and nasal administration by utilizing computational fluid dynamics (CFD)-based analysis of various design concepts.

The primary disadvantage of the air-jet DPI is that the high-velocity turbulent jet (which efficiently aerosolizes the powder) leads to losses when it leaves the device and enters the patient interface and ET regions (MT or NT). The high velocity of the jet from the outlet capillary imparts a large amount of momentum to the particles, which in turn causes a large amount of impaction deposition downstream of the device. This was clearly apparent from the impaction of the aerosol on the back of the MT model that was observed by Farkas et al. (6). The jet also tends to attach to the walls of the patient interface, due to the Coanda effect, which directs the aerosol towards deposition surfaces instead of traversing the MP or NC. As such, the flow pathway of the patient interface (MP or NC) should be engineered to dissipate the intensity of the jet to minimize system losses. Previous examples of this type of patient interface optimization include improvements in mouthpiece performance of a capillary aerosol generator (10), the use of co-flow spacers with low actuation-air-volume DPIs (11,12), and multiple design improvements to a mouthpiece coupled to the Aerolizer DPI (13,14).

The objective of this study was to explore different internal flow pathways for a pediatric air-jet DPI interface that minimizes device and ET depositional loss using validated CFD methods. The design space was constrained to an internal flow pathway less than 75 mm in length to provide a compact and portable device, and preference was given to design concepts that are easy to manufacture and construct. The performance target was total CFD-predicted losses in the flow pathway and ET region of less than 15% for a pediatric subject. Combining this target with approximately 10% device loss from Farkas et al. (6) results in an expected lung dose of greater than approximately 75% of loaded dose. Validated CFD models were used to evaluate several design iterations that aimed to screen candidate design concepts until the performance targets were met. A leading design concept explored in this study was the use of a 3D rod array, previously designed to maximize aerosol deaggregation (15–18), to attenuate the high-velocity air-jet that leaves the DPI and thereby reduce depositional losses in the interface and ET regions.

METHODS

Overview and System Setup

Overviews of flow passages for the pediatric air-jet DPI systems are shown in Fig. 1 for both oral and nasal aerosol administration. The air-jet DPI consists of an inlet orifice flow passage, aerosolization chamber, outlet orifice flow passage, and smooth expansion. The inlet and outlet orifice flow passages are frequently constructed with hollow metal capillaries and are therefore often referred to as inlet and outlet capillaries. As described by Farkas et al. (6) the air-jet DPI considered orients the inlet and outlet capillaries along the long axis of the aerosolization chamber and does not include bypass flow (straight-through design). The air-jet DPI is connected to the ET model (MT or NT) through the patient interface. For pediatric aerosol delivery conditions and the straight-through air-jet DPI design, Bass et al. (9) previously optimized the air-jet DPI design parameters to maximize aerosolization performance.

In the current study, the patient interface region is evaluated and optimized to reduce both interface and ET depositional losses. As described, a major source of this aerosol loss arises from the high-speed turbulent air-jet that enters the patient and ET region from the air-jet DPI outlet capillary. For this reason, the outlet capillary and expansion region are included in the pediatric interface models. The fundamental question of this study is then how to design the patient interface for oral or N2L aerosol administration that can attenuate a high-speed turbulent air-jet while also reducing depositional losses.

Considering the patient interface, potential designs are illustrated in Fig. 2 based on an axial cross-section and plane of symmetry. Potential design ideas include internal geometry control, wall surface characteristics, and internal flow structures, such as the 3D rod array. Wall geometries are intended to either avoid boundary layer separation (gradual expansion) or rapidly move the wall away from the expanding jet (rapid expansion). A rough wall surface is included to improve boundary layer attachment (*via* boundary layer "tripping"). Internal flow structures are intended to quickly dissipate the turbulent jet with minimal particle depositional loss.
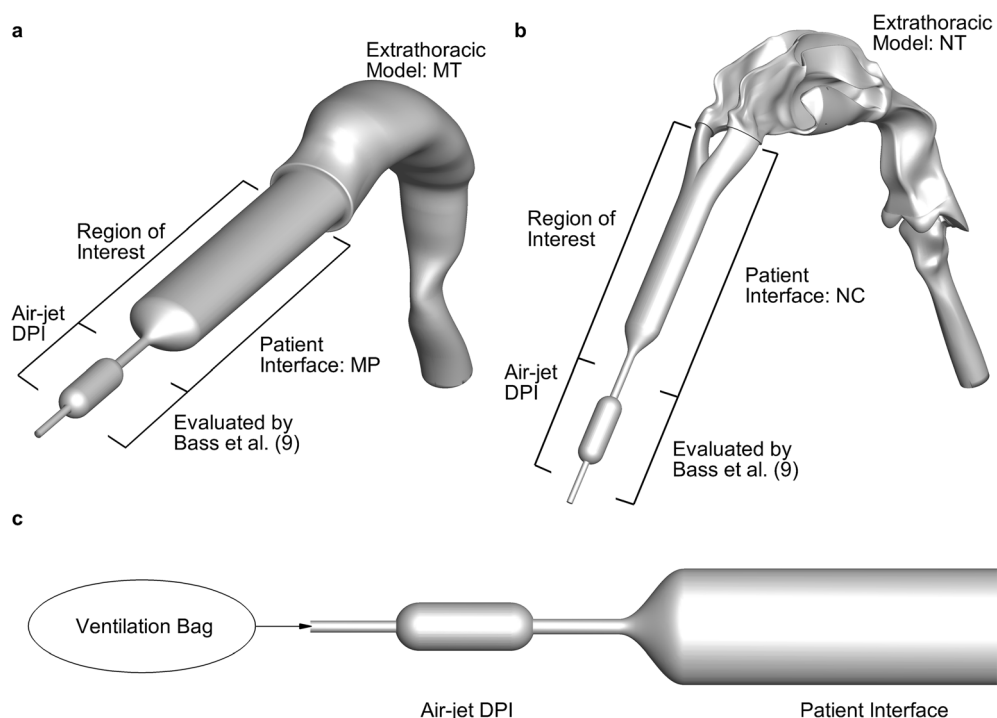
Fig. 1. Overview of delivery system and extrathoracic models for **a** oral administration *via* a mouthpiece (MP) through the mouth-throat (MT), **b** nasal administration *via* a nasal cannula (NC) through the nose-throat (NT), and **c** inclusion of the ventilation bag placement for actuation of the air-jet DPI. As noted in the figure, the air-jet DPI was previously evaluated by Bass et al. (9)

Evaluation Process

To achieve the study objective, the process outlined by the flow diagram in Fig. 3 was employed to evaluate numerous design concepts and assess the performance improvements of candidate patient interfaces. The primary aims of the evaluation process were to establish CFD-based predictive metrics for estimating the interface and ET depositional losses associated with each design concept and to improve device performance in terms of reducing these losses.

Following the process flowchart shown in Fig. 3, the CFD models for oral and nasal administration were first validated against the experimental data presented by Farkas et al. (6) for their best-case patient interfaces. Regional deposition efficiency (DE) in the patient interface (MP or NC) and extrathoracic regions (MT or NT) were compared between the CFD models and experimental data. Initially, meshing and solver parameters adhered to the recommendations from our previous work (19–21) and adjustments were made due to the specific requirements of this investigation, which are described in detail in subsequent sections. Validation focused on maximizing model accuracy with the MP-MT model, as it was used to screen the design concepts. Once model settings were established for the validated MP-MT model, they were not adjusted for subsequent models to ensure consistency between all cases considered.

With the model validation complete, the metrics to predict losses up to the first impaction point from CFD flow field quantities were developed (Fig. 3). This required correlation of the chosen metrics with CFD-predicted DEs in the region of interest to determine the strength of the metric for estimating interface performance. The intention of this approach is to model the patient interface flow pathway independently from the rest of the geometry to reduce processing times and increase the turnaround on screening design concepts. That is, evaluation of flow field quantities from a CFD model of only the MP or NC pathway can be used to predict depositional losses in the remainder of the geometry, which combined with CFD predictions of deposition in the patient interface can be used to efficiently determine performance improvements. Next, models of design concepts were developed and screened using CFD predictions of interface losses and the aforementioned deposition metrics (Fig. 3). Three design screen iterations were required to minimize system losses, with each iteration using insight from the last to improve performance and optimize the design (Fig. 3).

Finally, four MP designs from the screening stage were selected for testing in a full CFD model of the chosen interface coupled with the MT airway (Fig. 3). Here, the performance of each design is evaluated with CFD predictions of losses in both the MP and MT regions. Therefore, any inaccuracies that the deposition metrics may have in estimating losses in the MT are removed. The selected design concepts are then applied to the NC, and the combined NC-NT models are tested with full CFD models to assess the performance improvement for nasal administration. From the final four selected design concepts, the best-performing patient interfaces for oral and nasal administration were identified based on CFD predictions of patient interface and ET losses. These best-case designs will be experimentally tested to verify the performance improvements in a future study.
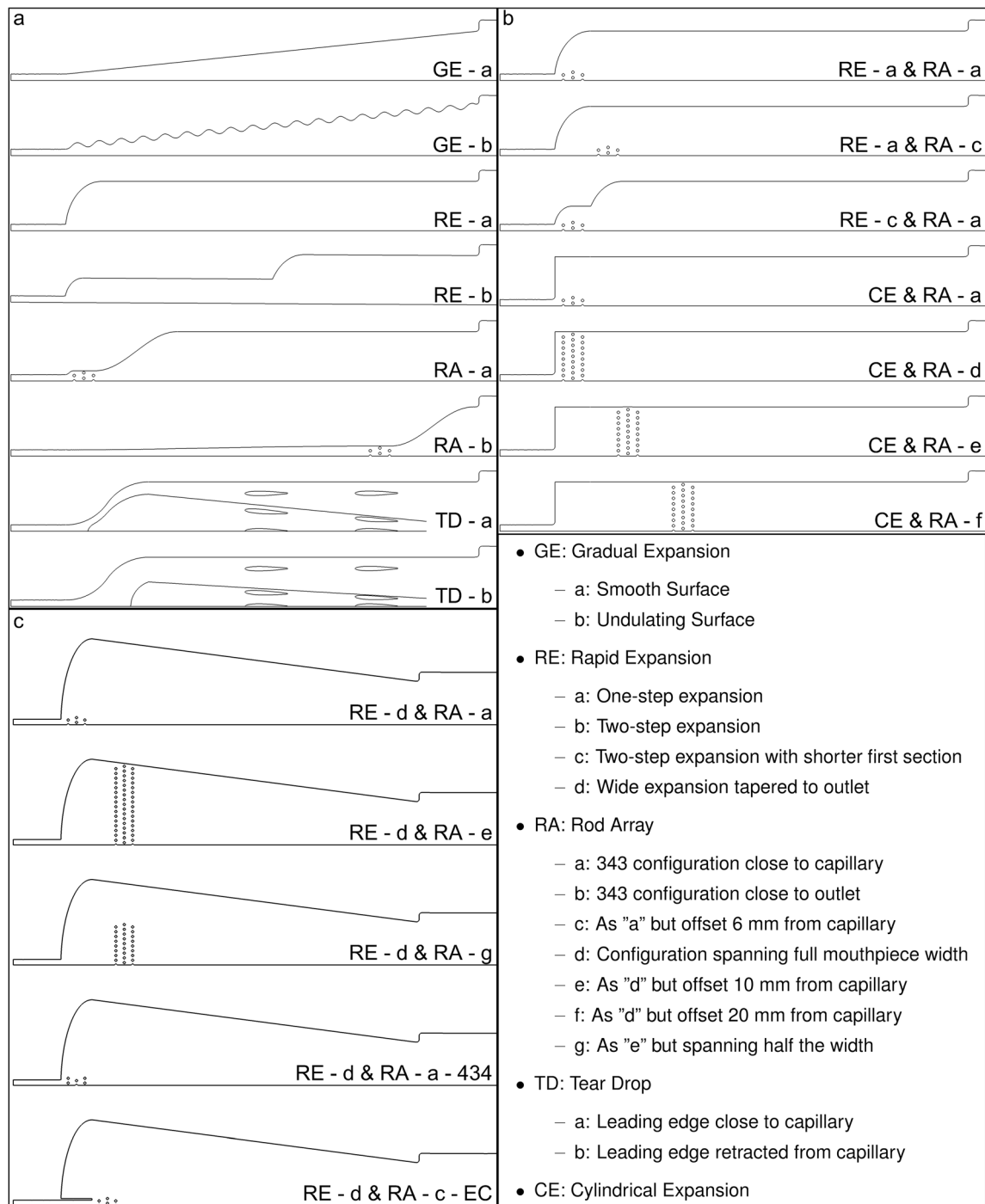
a

GE - a

GE - b

RE - a

RE - b

RA - a

RA - b

TD - a

TD - b

b

RE - a & RA - a

RE - a & RA - c

RE - c & RA - a

CE & RA - a

CE & RA - d

CE & RA - e

CE & RA - f

c

RE - d & RA - a

RE - d & RA - e

RE - d & RA - g

RE - d & RA - a - 434

RE - d & RA - c - EC

- **GE: Gradual Expansion**
  - a: Smooth Surface
  - b: Undulating Surface
- **RE: Rapid Expansion**
  - a: One-step expansion
  - b: Two-step expansion
  - c: Two-step expansion with shorter first section
  - d: Wide expansion tapered to outlet
- **RA: Rod Array**
  - a: 343 configuration close to capillary
  - b: 343 configuration close to outlet
  - c: As "a" but offset 6 mm from capillary
  - d: Configuration spanning full mouthpiece width
  - e: As "d" but offset 10 mm from capillary
  - f: As "d" but offset 20 mm from capillary
  - g: As "e" but spanning half the width
- **TD: Tear Drop**
  - a: Leading edge close to capillary
  - b: Leading edge retracted from capillary
- **CE: Cylindrical Expansion**

Fig. 2. Overview of patient interface design concepts for **a** screening iteration 1, **b** screening iteration 2, and **c** screening iteration 3

CFD Models

Computational Domains and Spatial Discretization

The MT and NT models used in the original experimental work (6) were the scaled 5–6-year-old VCU MT geometry (22,23) and the realistic pediatric NT geometry from the RDD Online website (www.rddonline.com), respectively. These models were selected for the experimental study as their geometric characteristics were consistent with the 5–

6-year-old age group (6) considered by the device design process. The computational geometries were created by importing these ET airways into SolidWorks 2018 (Dassault Systèmes, Paris, France) and using its 3D modeling capabilities to combine the MT or NT models with either the MP or NC patient interfaces, respectively. To maintain consistency between the experimental and computational models, the NC prongs were inserted 5 mm into the NT model and surfaces near the prong outlets were modified to provide an air-tight seal between the NC and nostrils. As such, there is no flow
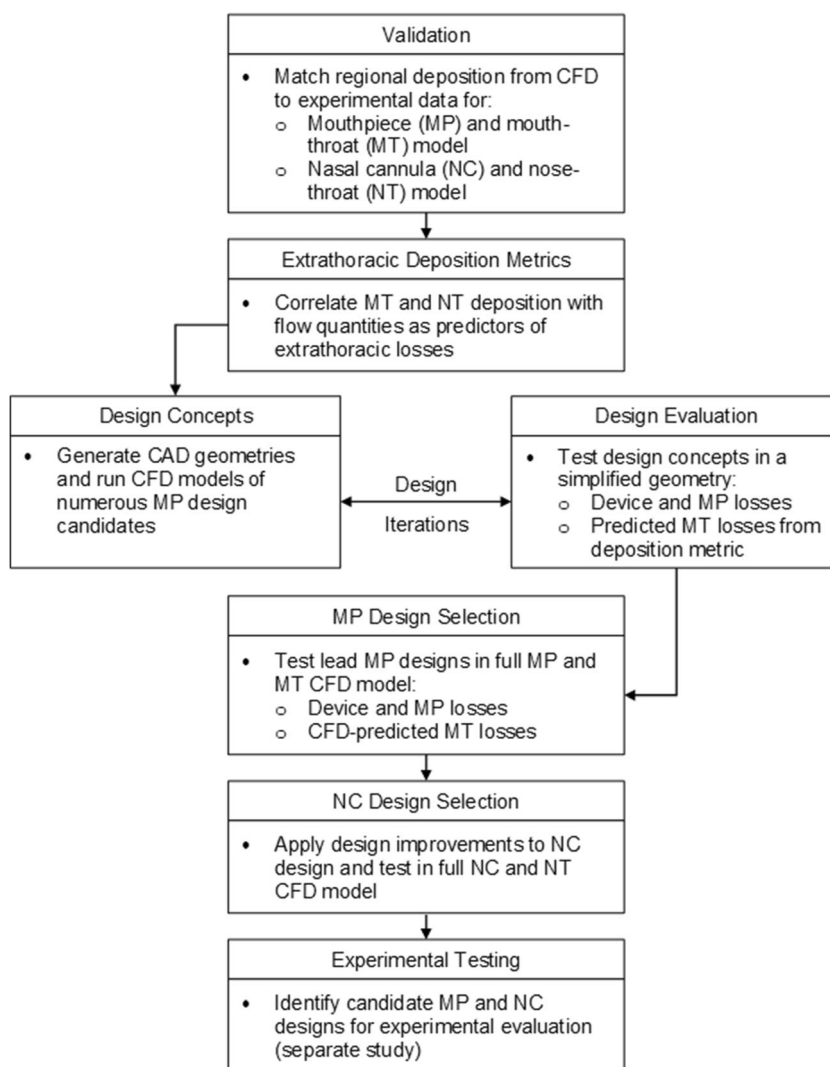
Validation

- Match regional deposition from CFD to experimental data for:
  - Mouthpiece (MP) and mouth-throat (MT) model
  - Nasal cannula (NC) and nose-throat (NT) model

Extrathoracic Deposition Metrics

- Correlate MT and NT deposition with flow quantities as predictors of extrathoracic losses

Design Concepts

- Generate CAD geometries and run CFD models of numerous MP design candidates

Design Iterations

Design Evaluation

- Test design concepts in a simplified geometry:
  - Device and MP losses
  - Predicted MT losses from deposition metric

MP Design Selection

- Test lead MP designs in full MP and MT CFD model:
  - Device and MP losses
  - CFD-predicted MT losses

NC Design Selection

- Apply design improvements to NC design and test in full NC and NT CFD model

Experimental Testing

- Identify candidate MP and NC designs for experimental evaluation (separate study)

Fig. 3. Process flow chart to evaluate design concepts with the objective of minimizing losses in the patient interface

through the nostrils around the prongs, as the device is designed to provide the full inhalation volume to the subject during actuation. Similarly, the MP is centrally located within the inlet to the MT model with an air-tight seal, which is consistent with the patient's lips surrounding the MP during actuation. 3D models were transferred to SpaceClaim v19.0 (ANSYS Inc., Canonsburg, PA) where surface preparation and minor geometry simplifications were made to facilitate the CFD meshing process, such as the removal of small area faces, filleting sharp edges, and the addition of numerical extensions.

Mesh generation (*i.e.*, the volume discretization of the computational domain) was performed by using the meshing capabilities available in FLUENT v19.0 (ANSYS Inc., Canonsburg, PA). Due to the complexity of the geometries that include rod arrays, an unstructured meshing approach was taken to accurately resolve the complex model surfaces. Polyhedral cell topology, with prismatic near-wall (NW) cell layers, was utilized throughout the patient interface and ET region in all models, as we have previously shown that these types of cells are more computationally efficient than traditional tetrahedral cells and provide accurate deposition

results [19]. The NW mesh resolution was consistent with our previously established best practices [20], which include a wall y^+ value of approximately one, five prismatic NW layers, and layer-to-layer growth ratio of 1.2. Final evaluation of all meshes ensured the orthogonal quality metric was greater than 0.25, with cell nodes smoothed until this threshold was achieved, which ensures a high-quality volume discretization.

Mesh independence was established for the MT and NT validation cases using the Roache method for grid refinement studies [24] by evaluating volume-averaged velocity magnitude (v_{mag}) and turbulent kinetic energy (k) between successively higher-resolution meshes. Throughout the mesh independence study, solutions were checked to ensure they were within the asymptotic range of convergence for which the Roache method is valid. For the MT model, three meshes with approximately 0.5, 1.0, and 2.0 million cells were evaluated, which gave normalized grid spacing ratios of 1.60, 1.32, and 1.00, respectively. Between the 2.0- and 1.0-million cell cases, the grid convergence index (GCI) for v_{mag} and k was 0.07% and 1.54% respectively, which suggests the estimated error from the 1.0-million cell case was low and acceptable for use with this study. For the NT model, higher-

resolution meshes compared to the MT model were required due to the increased model complexity, with meshes using approximately 1.0, 2.0, and 4.0 million cells, which gave normalized grid spacing ratios of 1.58, 1.25, and 1.00, respectively. Between the 4.0- and 2.0-million cell cases, the GCI for v_{mag} and k was < 0.001% and 8.75%, respectively. Ideally, the GCI for k in the NT model would be less than 5%, but given that v_{mag} shows a very low estimated error and particle trajectories in the micrometer size range are more heavily influenced by the velocity field than the turbulence field, the 2.0-million cell case was deemed acceptable. Subsequent meshes used in the evaluation of new patient interface designs use similar cell sizes to these validation cases, as opposed to similar cell counts, to ensure the spatial resolution is consistent between models.

Numerical Modeling and Solver Settings

The Mach and Reynolds numbers at the inlet to the patient interface, given a flow rate of 13.3 LPM and inlet capillary diameter of 2.39 mm (6), are 0.14 and 5200 respectively, which suggest incompressible and transitional-to-turbulent flow conditions. As such, a constant density for the fluid phase was implemented, in contrast to the ideal gas law in previous studies (7–9), which had a much smaller inlet jet diameter, as the Mach number is far below the critical value of 0.3 for compressible flow. To model the transitional-to-turbulent flow regime, the low-Reynolds number (LRN) k-ω turbulence model was used, which has been validated by our group for both the evaluation of DPI performance (18) and particle transport through ET airways (19–21) for adults and children. The formulation of the LRN correction to the k-ω model includes an eddy viscosity damping coefficient that scales from 0 to 1 in regions of low or high turbulence, which improves solution accuracy outside and inside the highly turbulent jet. Considering the inlet jet, the shear flow corrections sub-model available in FLUENT v19.0 was applied to model the shear layer between the high-velocity jet and relatively quiescent flow in the patient interface.

Using a steady-state solution approach, preliminary work on the validation cases showed the inlet jet would attach to the wall of the patient interface and move around the domain with erratic behavior, which prevented convergence of the transport equations. Therefore, a transient formulation of the transport equations was implemented to model the transient nature of the inlet jet development. The flow was initialized with quiescent conditions, and the boundary conditions at the inlet cause the jet to propagate into the patient interface. As with the preliminary work, the jet attaches to the walls and wanders unpredictably in all cases considered, due to the Coanda effect. The transient solution approach used a time step of 1e−3 s, which gave good flow field convergence within 100 iterations per time step, and sufficiently resolved the inlet jet behavior. Also, during preliminary work, observation of regional DE *vs.* time plots showed that the total and regional deposition converged to a single value within 0.45 s, which determined the maximum required simulation time, as an alternative to modeling the full actuation time of 3 s. These transient solver settings and the mesh independent spatial discretization resulted in processing times of between 24 and 72 h (on 10 CPUs) depending on the cell count.

FLUENT v19.0 (ANSYS Inc., Canonsburg, PA) was used to obtain solutions for all flow and turbulence equations, including the LRN k-ω turbulence model and shear flow corrections. As with the mesh generation step, all solver settings followed our recommendations for modeling particle transport in DPIs and the respiratory airways (19,20). Specifically, the Green-Gauss Node-based method for gradient discretization, which combined with the NW mesh resolution requirements mentioned previously, provide an improvement in grid independence in the NW region and improved consistency and accuracy in particle deposition data. The spatial discretization of flow and turbulence equations was second-order accurate, while the standard pressure interpolation scheme was used. Convective terms used a second-order upwind scheme and diffusion terms used central difference. Further details on the mass, momentum, and turbulence transport equations are available in other publications (25,26).

A mass flow inlet condition was utilized at the inlet flow boundary to the patient interface, with a mass flow rate that gave a volumetric flow rate of 13.3 LPM, which is consistent with the volumetric flow rate through the Case 4 DPI presented by Farkas et al. (6). A 10-mm length of the device outlet capillary (inlet to the patient interface) was included in the model to allow the flow to reach a fully developed state before entering the MP or NC. A pressure outlet condition was used at the outlet of the ET airway model, with gauge pressure (relative to ambient pressure) set to 0 kPa. To minimize the influence of the pressure outlet on the flow field in the ET models, a 60-mm numerical extension was added to the outlet in the CFD domain. All wall boundaries in the CFD model use the no-slip shear condition and the effects of surface roughness on the flow field and particle trajectories were neglected. Wall boundaries of the 3D-printed components used the trap discrete phase model (DPM) boundary condition such that any particle that contacts these walls is assumed to deposit on the boundary. Wall boundaries of stainless-steel components used the reflect DPM boundary condition, with default coefficients of restitution, which assumes particles bounce off of these surfaces.

Particle Trajectories and Deposition Calculations

Particle trajectories were calculated with the DPM available in FLUENT v19.0 (ANSYS Inc., Canonsburg, PA), with the Runge-Kutta scheme used to integrate the particle equations of motion, which is dependent on the underlying flow and turbulence field quantities. Settings for the DPM follow our best practices (19,20,27,28), which have been successfully validated against experimental deposition data. Microparticle trajectory calculations with the DPM and LRN k-ω turbulence approximation generally over-predict deposition when compared to experimental data, due to the assumption of isotropic NW turbulence and the associated fluctuating velocity components. As such, Longest and Xi (27) proposed corrections to the NW flow and turbulence fields extending work by Matida et al. (29) and Wang and James (30), which are implemented in FLUENT *via* user-defined functions (UDFs). In summary, the NW corrections interpolate the velocity field from the cell centroid to the particle location, implement anisotropic fluctuating velocity components, and damp the wall-normal velocity to approximate particle-wall hydrodynamic interactions. These NW

corrections use a NW limit control parameter that determines the wall-normal distance, below which the wall-normal velocity is damped. Previous validation work (19,20) showed that a NW limit of 1–2 μm was suitable for modeling microparticle deposition the upper airways, with a value of 2 μm used in the present study.

Particles were introduced into the model at the inlet to the air-jet DPI outlet capillary (*i.e.*, the inlet to the CFD domain) with a blunt spatial distribution, as the inlet Reynolds number suggests the flow is in the transitional to turbulent regime. Initial particle velocities also followed a blunt profile based on each particle's radial location relative to the circular boundary. A polydisperse aerosol was used in the CFD models, with the particle size distribution determined by next-generation impactor (NGI) characterization at the Case 4 device outlet presented by Farkas et al. (6). Particle deposition convergence was ensured by following the recommendations from Tian et al. (31) with 100 particles per bin per time step, which resulted in 360,000 total particles (considering eight NGI bins and 450 time steps).

Regional particle deposition in the device, interfaces, and ET models are compared *via* DE, which is the ratio of particles that deposit in a given region to number of particles that enter that region. To convert the DE from the CFD models (with a constant number of particles per bin) to a DE that is consistent with the experimentally determined particle size distribution, the CFD-predicted DE for each NGI bin is multiplied by the mass fraction of particles for each bin, and then summed over all bins. This is defined as

$$DE_i = \frac{n_i}{N_i} \tag{1}$$

$$\varphi_i = \frac{m_i}{M} \tag{2}$$

$$DE_r = \sum_{i=1}^{8} DE_i \times \varphi_i \tag{3}$$

where n_i is the number of particles that deposit in the region for bin i, N_i is the number of particles the enter the region for bin i, DE_i is the DE for bin i, m_i is the mass of particles from the NGI characterization for bin i, M is the total aerosol mass, φ_i is the mass fraction for bin i, and DE_r is the DE for a given region. To determine the mass or number of particles that enter the region, the mass or number of particles that deposit in upstream regions is subtracted from the injected aerosol conditions. Finally, the total deposition fraction (DF) for the entire domain, which is the ratio of particles that deposit in the domain to the particles that enter the domain, can be calculated from the regional DE as follows:

$$DF_{Tot} = 1 - \prod(1 - DF_r) \tag{4}$$

Deposition Metrics

Figure 4a and b show the separation of the MP flow pathway from the MT, and Fig. 4c and d show the separation of the NC flow pathway from the cannula bifurcation and NT. The NC was split just upstream of the bifurcation as the objective of the study was to evaluate interface designs that reduce the losses associated with the high-velocity jet from the device outlet, and preliminary work showed that losses in the NT region were not affected by changes to the jet intensity. That is, reducing the intensity of the inlet jet to the NC did not reduce ET losses, but deposition on the bifurcation was reduced, which suggests the potential for improvements in interface losses. Put another way, the inlet jet causes impaction deposition on the first surface that it encounters when it leaves the device outlet capillary. In the MP-MT model, this impaction surface is the back of the mouth-throat and the model is split between the MP and MT regions. In the NC-NT model, this impaction surface is the NC bifurcation and the model is split between these two regions.

ET deposition metrics were evaluated by applying four different velocity profiles to the MT and NT models at the inlets labeled in Fig. 4b and d, respectively. These four velocity profiles were named the jet (u_{Jet}), turbulent (u_{Turb}), laminar (u_{Lam}), and intermediate (u_{Int}) profiles, and are plotted graphically in Fig. 5a. The functions that define each profile are

$$u_{Jet} = u_{max} \times \exp\left[-\frac{(r/R)^2}{2\sigma^2}\right] \tag{5}$$

$$u_{Turb} = u_{max} \times \left(1 - \frac{r}{R}\right)^{1/7} \tag{6}$$

$$u_{Lam} = u_{max} \times \left(1 - \left(\frac{r}{R}\right)^2\right) \tag{7}$$

$$u_{Int} = \frac{u_{Jet} + u_{Turb}}{2} \tag{8}$$

where u_{max} is the peak velocity, r is the radial location on the inlet boundary, and R is the maximum radius of the inlet boundary. Using the r/R definition for the radial location on the inlet boundary simplified the conversion from circular to elliptical coordinates for the inlet to the MT model. The u_{Jet} profile uses a Gaussian function to define the jet-type profile seen in Fig. 5a, with u_{max} determined from time-averaged peak velocity from the oral and nasal validation cases and σ selected to provide a volumetric flow rate of 13.3 LPM consistent with the Case 4 DPI (6). The u_{Turb} profile uses the 1/7th power law for a turbulent profile (32); the u_{Lam} profile uses the analytical solution for laminar flow; and the u_{Int} profile is simply the average of the u_{Jet} and u_{Turb} profiles. The combination of flow profiles considered represents a wide range of potential flow conditions that may enter the MT or NC interface depending on inhaler design. For the air-jet DPI, the turbulent high-velocity jet most likely best represents conditions when the air-jet exiting the DPI is not dissipated. At the other extreme, the laminar flow profile represents conditions that may occur if the air-jet is not present or is fully dissipated through optimal design of the patient interfaces.
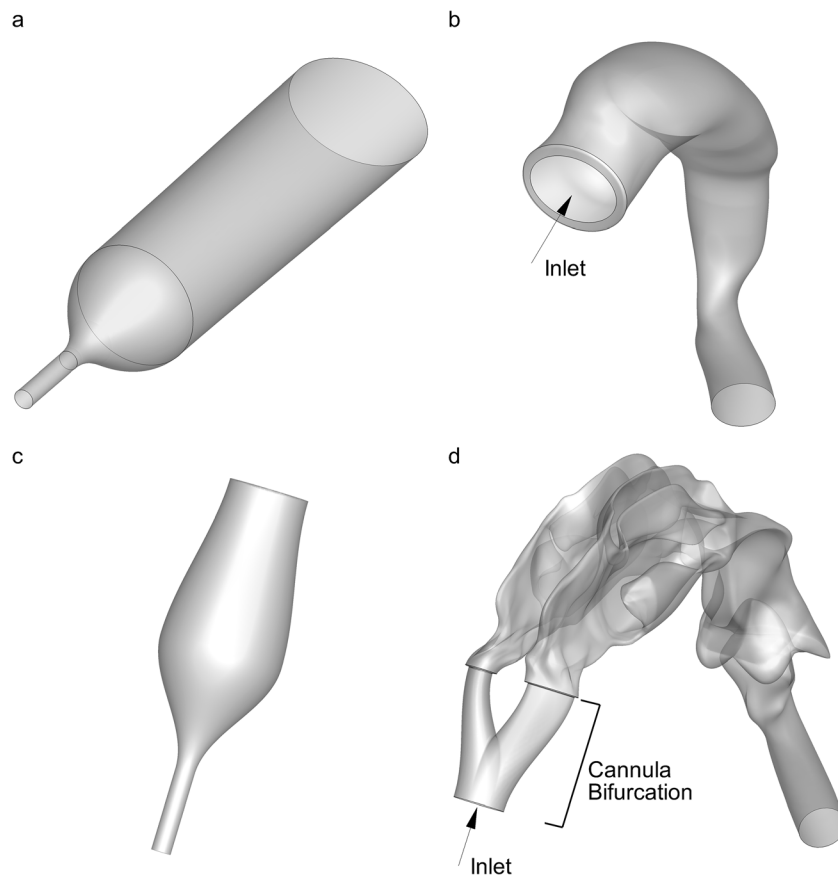
Fig. 4. Overview of model geometry showing **a** mouthpiece flow pathway, **b** mouth-throat only model, **c** nasal cannula flow pathway, and **d** nose-throat and cannula prongs model for evaluation of deposition metrics
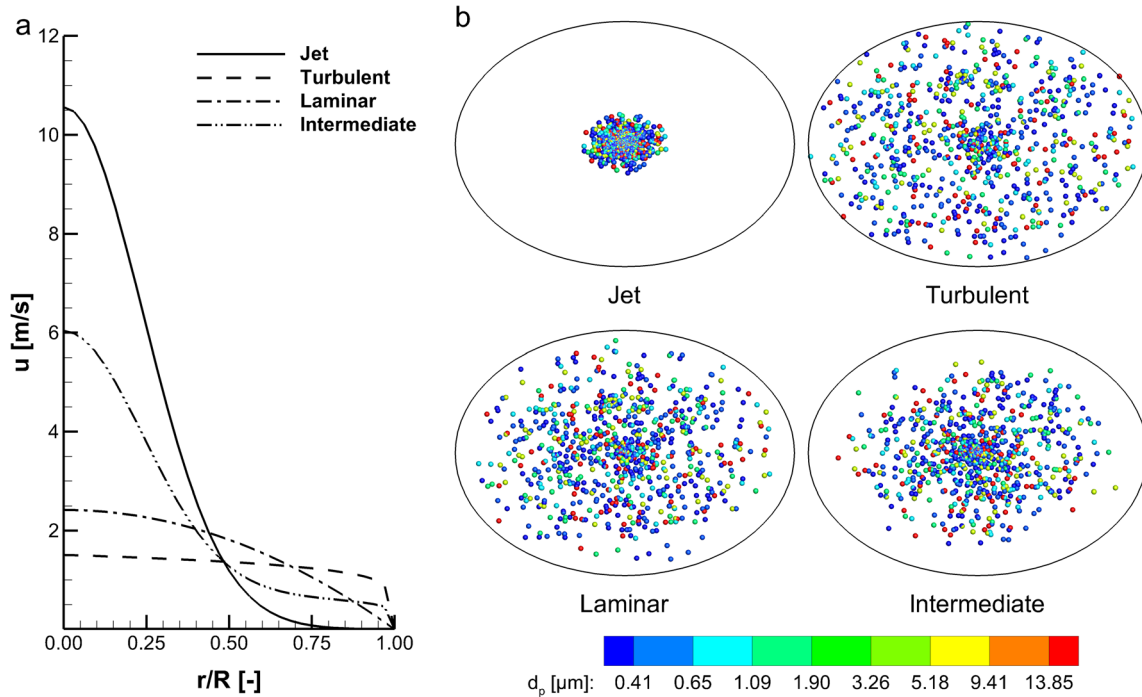

Fig. 5. Boundary conditions used to establish extrathoracic deposition metrics in the mouth-throat models showing **a** velocity profiles applied at the inlet boundary and **b** spatial distribution of initial particle locations (nose-throat models used similar boundary conditions)

To determine the particle spatial distribution profile, each velocity profile was treated as a probability density function (PDF) and split into 32 equally spaced rings, with particles randomly assigned to each ring based on the PDF. This method of defining particle spatial distributions is similar to that described by Longest and Vinchurkar (33), but applied to the four profiles used to evaluate ET deposition metrics. The resulting spatial particle distribution for each MT of NC inlet velocity profile is shown in Fig. 5b.

Observations from the experimental work presented by Farkas et al. (6) demonstrated a large amount of deposition on the back of the throat in the pediatric MT model. Therefore, initial work on predicting ET loss aimed to describe the intensity of the jet as it enters the MT or NT model. Specifically, these metrics were the peak velocity, velocity spread, and uniformity index, which were all evaluated on the plane between the patient interface and ET region. Peak velocity is simply the time-averaged maximum velocity on the sampling plane, velocity spread is the standard deviation of velocity on the plane, and uniformity index (UI) is given as

$$UI = 1 - \left(\frac{\sum_{i=1}^{N} \left(\left| u_i - \overline{u} \right| \times A_i \right)}{2 \times \overline{u} \times A} \right) \tag{9}$$

where u_i is the velocity on face i, $\overline{u}$ is the area-average velocity, A_i is the area of face i, and A is the total plane area. A UI with a value close to one describes a uniform flow velocity, such as the u_{Turb} profile, whereas a value closer to zero describes non-uniform flow velocity, such as the u_{Jet} profile.

RESULTS

CFD Model Validation

Deposition patterns presented in this study generally split the domain into three regions: the device outlet (outlet capillary and expansion), patient interface (MP or NC), and the ET region (MT or NT). For the purposes of model validation, regional DEs are compared between the CFD and experimental results in the patient interface and ET regions, with DEs on the device outlet provided for completeness. Figure 6a shows that CFD predictions of aerosol DE were in close agreement with the experimental (Exp) results in the MP and MT regions, with a maximum absolute error in regional DE of − 0.6% in the MT region. Total DF in the entire model also matched well between the CFD and experimental data with an absolute error of 0.2%. CFD results in the NC-NT model, presented in Fig. 6b, did not match as closely to the experimental data as with the oral model, but agreement was still considered acceptable. Maximum absolute error in regional DE was 5.1% in the NT region, and the CFD model over-predicted total DFs in the entire domain by 8.3%.
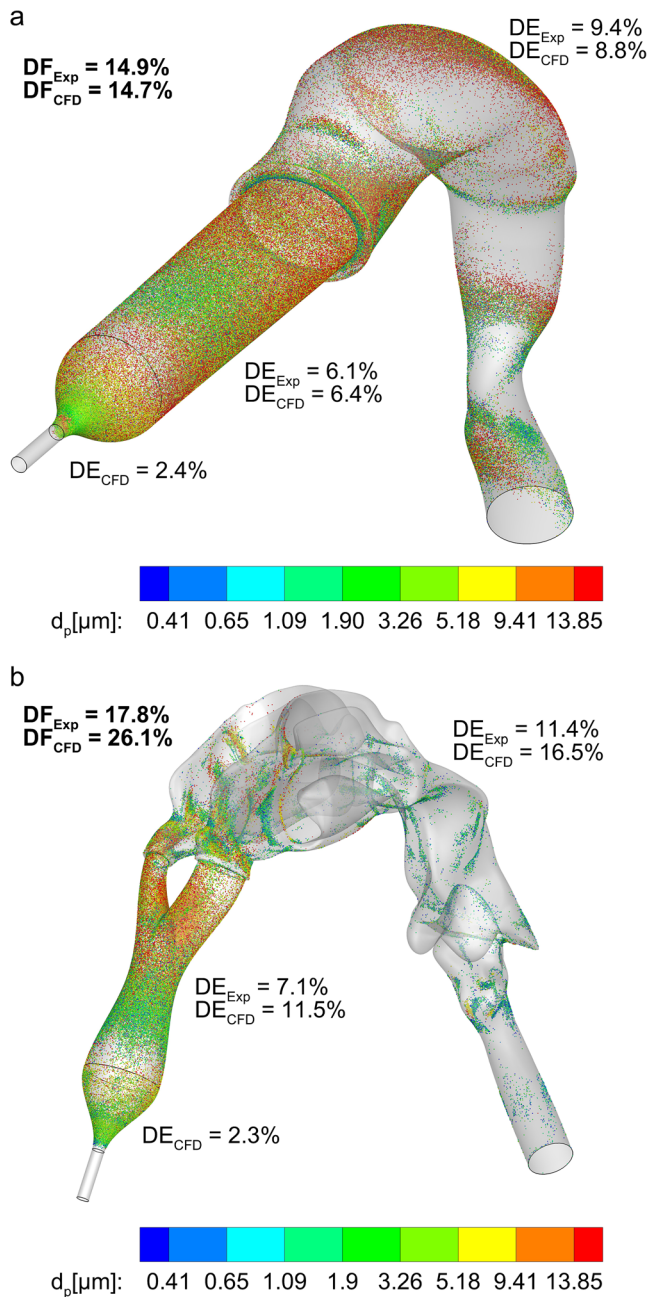
Fig. 6. Validation of CFD-predicted deposition with experimental data for **a** the mouthpiece and mouth-throat models and **b** the nasal cannula and nose-throat model

Deposition Metrics

Of the three deposition metrics described in the "Methods" section, correlating the time-averaged maximum velocity on the plane at the outlet of the flow pathway with MT (Fig. 7a) and NC (Fig. 7b) DE gave the best prediction of losses, with R^2 values greater than 0.95 and standard error ranging from approximately 0.5 to 0.6%. It is noted that the different velocity profiles considered all had the same volumetric flow rate. Therefore, deposition in the MT correlates with not only volumetric flow rate, but also the peak value of the velocity profile that enters the region. With such a strong correlation, further development of deposition
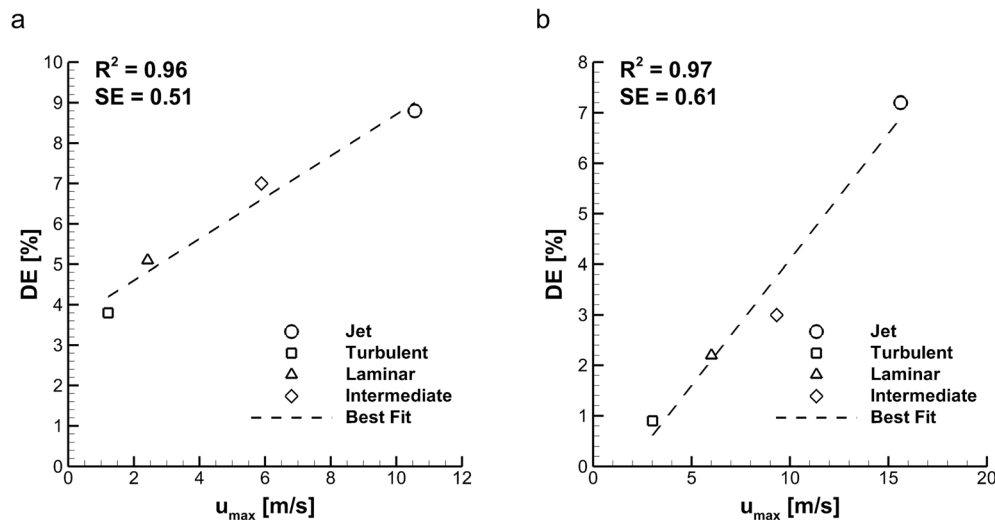
Fig. 7. Plots showing the correlation between time-average peak velocity at the patient interface outlet (u_{max}) and the deposition efficiency (DE) up to the first impaction point, which is **a** the back of the throat for the mouthpiece and mouth-throat model and **b** the bifurcation point for the nasal cannula and nose-throat model

metrics was not required. Figure 7a plots the DE in the MT region (Fig. 4b) against the maximum velocity at the MT inlet for the four imposed velocity profiles (Fig. 5a). Similarly, Fig. 7b plots the DE in the NC bifurcation region (Fig. 4d) against the maximum velocity at the inlet for the same velocity profiles. As mentioned previously, the NC-NT model was split into the domains shown in Fig. 4c and d as preliminary work showed that imposing velocity profiles at the inlets of the NT region (outlet of the NC prongs) had little influence on reducing ET losses. However, the deposition metrics show that reducing the intensity of the jet entering the NC bifurcations (as quantified by peak velocity) can reduce interface losses at the first impaction point, just as in the MT with oral aerosol delivery.

Figure 8 shows the deposition patterns in the MP-MT model when the jet (Fig. 8a) and turbulent (Fig. 8b) velocity profiles were imposed at the inlet. Figure 8a shows a large amount of impaction deposition on the back of the MT, due to the high-velocity jet entering the region, which was also observed experimentally by Farkas et al. (6). In Fig. 8b, this impaction region was minimized as the intensity of the inlet jet was vastly reduced with the turbulent velocity profile, which leads to a reduction in MT losses from 8.8 to 3.8% at the same volumetric flow rate. In the laryngeal region of the pediatric MT model, deposition patterns were similar between the jet and turbulent profile cases as inlet effects are less apparent downstream in the domain. Similarly, Fig. 8c and d show the deposition patterns in the NC-NT model for the jet and turbulent velocity profiles, respectively. As with the MT model, minimizing the inlet jet intensity reduces the losses at the first impaction point, which in the NC-NT model is the cannula bifurcation, from 7.2 to 0.9%. However, there is little difference in NT losses when imposing different velocity profiles, with DEs ranging from 19.2 to 19.7%. This supports the insight from the preliminary work and deposition metrics that NT losses are difficult to minimize with changes to the design of the NC flow pathway, but NC interfaces losses can be improved.

Design Concept Screen 1

Diagrams that illustrate the MP design concepts in the first iteration were presented in Fig. 2a. These diagrams provided an axial mid-plane slice of the interface aligned with the top-down view and show the MP geometry along with any internal components. The first iteration implemented four design concepts, with two variations of each concept. The gradual expansion (GE) concept steadily increased the MP diameter from the circular outlet capillary to the elliptical MP outlet. The variations of the GE concept used a smooth (a) and an undulating (b) surface, with the intention being that the undulating surface would increase turbulence through tripping the boundary layer, thereby keeping the flow attached and preventing recirculation. The rapid expansion (RE) concept quickly transitions from the outlet capillary diameter to the elliptical MP cross-section with a dome shape that extends 6.5 mm from the capillary. The variations of the RE concept used a one-step (a) and two-step (b) expansion, where the two-step expansion initially transitioned to an elliptical cross-section that had half the radii lengths of the outlet over the first half of the MP length. The intent of the two-stage RE variation was to determine whether the MP cross-section should be increased incrementally to dissipate the intensity of the inlet air-jet. The rod array (RA) concept used 0.5-mm diameter rods arranged in a 3-4-3 configuration and placed in the flow pathway to break up the high-velocity inlet jet and reduce its intensity. The variations of this design concept placed the rod array close to the outlet capillary (a) or close to the MP outlet (b) to provide insight on the optimal positioning of the rod array. Finally, the tear drop (TD) concept placed a streamlined obstacle in the flow pathway to both break up the inlet jet and minimize recirculation by keeping the flow attached to the outer wall of the MP. The tear drop was suspended in the flow pathway with six supports that were placed in a triangular arrangement and followed a National Advisory Committee for Aeronautics (NACA) 0012 profile to reduce their influence on the flow
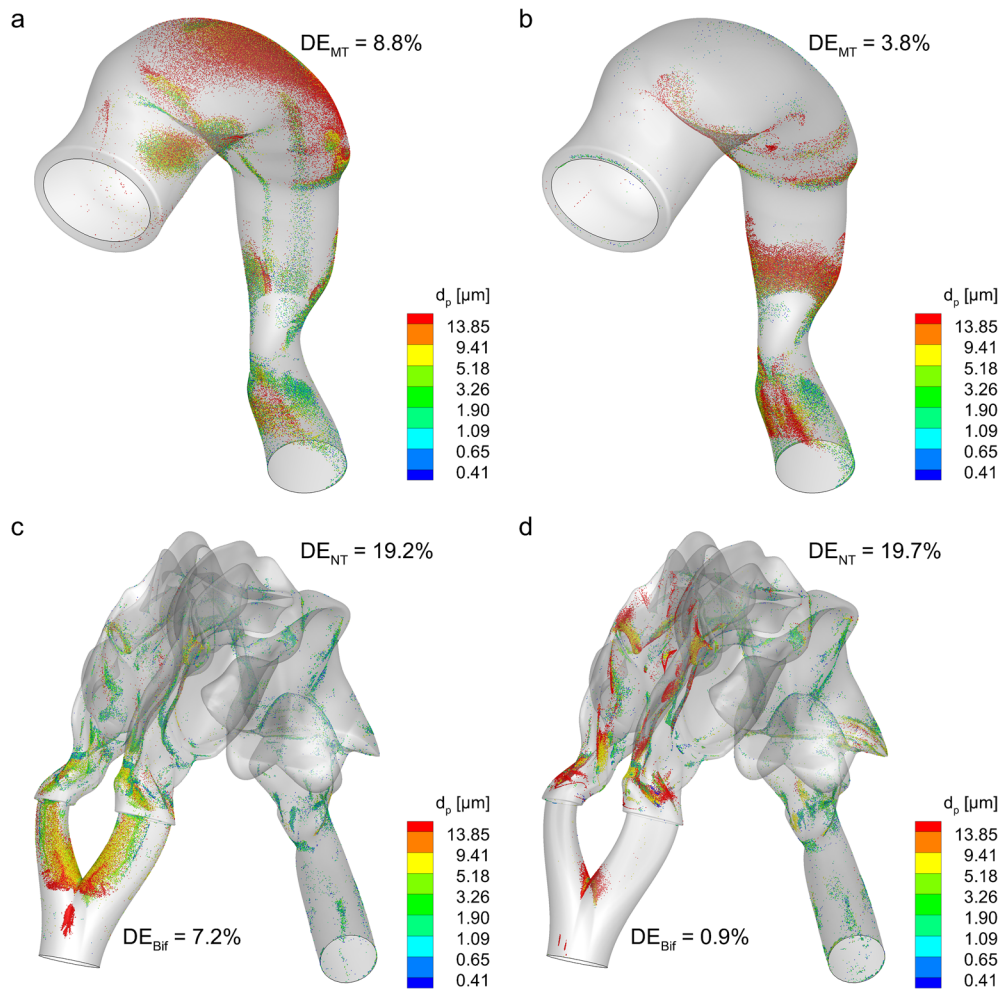
Fig. 8. Particle deposition patterns in the **a** mouth-throat (MT) region with the jet inlet velocity profile, **b** MT region with the turbulent inlet velocity profile, **c** nose-throat (NT) and bifurcation (Bif) region with the jet inlet velocity profile, and **d** NT and Bif region with the turbulent inlet velocity profile

field as much as possible. The variations of this design concept used a tear drop shape that extended into the transition region between the outlet capillary and MP and another design that moved the leading edge of the tear drop away from the outlet capillary. The intent of these two variations was to determine the effects on impaction deposition by moving the blunt edge of the tear drop away from the jet source.

Tables I and II, used in conjunction with Fig. 2a, present the CFD-predicted losses on the device outlet (DE_{Dev}) and patient interface (DE_{MP}), and the correlation-predicted MT losses (DE_{MT}) for the eight MP designs described above. The GE cases both reduced peak velocity at the MP outlet, which suggests an improvement in MT losses based on the deposition correlation. However, the interface losses for both variations of the GE concept were high (34.4% and 17.0%) compared to the original MP design (6.4%). It is interesting to note that the undulating surface (GE-b) reduced the CFD-predicted MP losses by approximately half compared to the smooth surface (GE-a). The RE design concept also reduced peak velocity and the associated MT losses, with the added benefit of a reduction in CFD-predicted interface losses compared to the original MP design of 6.4 to 1.8%. The RE-a design gave the best performance improvement of all

eight cases considered in the first iteration, with the total domain DF reduced from 16.7 to 11.8%. The RA-a case gave the best reduction in peak velocity and estimated MT losses of all cases evaluated in the first iteration, from 8.8% to a predicted 4.9% comparing the original MP and RA-a designs respectively. The two TD cases performed well in terms of minimizing flow recirculation, reducing device outlet losses, and predicted MT losses, but a large amount of impaction deposition on the leading-edge caused very high MP losses

Table I. Summary of experimentally determined patient interface and extrathoracic deposition efficiencies and fractions (based on air-jet DPI emitted dose) from Farkas et al. (6) for the best-case mouthpiece and nasal cannula devices. Experimental values are given as means with standard deviations shown in parenthesis [n=3].

Region	Mouthpiece [%]	Nasal Cannula [%]
Interface DE	6.1 (0.7)	7.1 (1.7)
ET DE	9.4 (1.6)	11.4 (3.5)
Total DF	14.9 (2.1)	17.8 (4.9)

DE Deposition efficiency, *DF* Deposition fraction, *ET* Extrathoracic

Table II. Comparison of peak velocity (Peak Vel.), predicted regional deposition efficiencies (DE) in the device (Dev), mouthpiece (MP), and mouth-throat (MT), and predicted total deposition fraction (DF$_{Tot}$) between the original mouthpiece and Design Screen 1

Case	Peak Vel. [m/s]	DE$_{Dev}$ [%]	DE$_{MP}$ [%]	DE$_{MT}$ [%]	DF$_{Tot}$ [%]
Original MP	10.5	2.4	6.4	8.8[a]	16.7
Design Screen 1					
GE-a	4.1	NA[b]	34.4	5.6	38.1
GE-b	4.7	NA[b]	17.0	6.0	21.9
RE-a[a]	5.0	4.4	**1.8**	6.1	**11.8**
RE-b	3.9	14.0	15.9	5.5	31.7
RA-a[d]	2.7	27.7	7.7	**4.9**	36.5
RA-b	19.3	50.5	1.0	13.6	57.6
TD-a	3.7	0.8	57.0	5.4	59.7
TD-b	2.6	0.6	54.7	4.8	57.1

GE Gradual Expansion, *RE* Rapid Expansion, *RA* Rod Array, *TD* Tear Drop

[a] Deposition efficiency for the Original MP case is from CFD-predicted particle trajectories, whereas deposition efficiency for all other designs is predicted from peak velocity at the mouthpiece outlet
[b] The gradual expansion cases go straight from the device outlet capillary to the mouthpiece, hence there is no device loss
[c] The RE-a case gave the best reduction in device and MP losses from Design Screen 1
[d] The RA-a case gave the best reduction in MT losses from Design Screen 1

(57.0% and 54.7%). Based on the results from Design Screen 1, a combination of the benefits observed for the RE and RA type designs may be utilized to improve patient interface performance in Design Screen 2. That is, the 3D rod array can be added to the RE geometry to both give an improved reduction in jet intensity, interface depositional loss, and predicted MT loss.

Design Concept Screen 2

The second iteration of design screening combined aspects of the RE and RA designs from the first iteration, and also introduced the cylindrical expansion (CE) geometry as an alternative to RE, as illustrated by Fig. 2b. The RE-a + RA-a design combines the geometry from the one-step variation of the RE concept with the rod placement and configuration from the first RA variation in an attempt to leverage the benefits of both designs from the first design screen iteration. RE-a + RA-c is similar to RE-a + RA-a with the rod array moved 6.5 mm downstream of the outlet capillary to gain insight into the placement of the rod array and its effect on losses. RE-c + RA-a uses a two-step expansion with a shorter first section than RE-b, and the first rod array variation, to evaluate the effect of keeping the flow constrained as it passes through the rods. CE + RA-a is similar to RE-a + RA-a except it uses the cylindrical-type geometry to provide a direct comparison between the combined RE + RA with the CE + RA design concepts. The final three designs in the second screening iteration (CE + RA-d/e/f) use the cylindrical geometry with rod arrays that span the full width of the MP with the intention of preventing the jet from reaching and attaching to the walls, as well as reducing the intensity of the jet. The three rod arrays are

located at 1.5, 10, and 20 mm from the outlet capillary to evaluate the depositional losses as the rod array is moved away from the source of the inlet jet.

Based on the deposition results in Table III, adding the RA to the RE geometry had the desired effect of improving MT losses by reducing the peak velocity of the inlet jet, which brings the total DF below the target of 15% (see italicized DF$_{Tot}$ values). However, the deflection of the jet due to the rod array causes higher interface losses, when compared to the RE-a case, as the flow is directed towards the side walls of the MP. Moving the RA further away from the capillary outlet in the RE-a + RA-c case leads to relatively high MP losses as the inlet jet flowed around the rods and attached to the walls instead of passing through the rod array and diffusing. Of all the design concepts considered in the second iteration, RE-c + RA-a had the worst performance in terms of flow pathway losses due to the close proximity of the interface walls to the rod array. That said, this case provides valuable insight as it shows that positioning the MP walls further away from the rod array reduces patient interface losses, which is explored further in the third design screen iteration. The CE + RA-a case had very similar performance to RE-a + RA-a, which shows that the slight change in the MP geometry has little effect on reducing depositional losses. The final three CE design concepts with rod arrays that span the full width of the interface also all had a similar level of performance (13.1–14.4% total DF). They show that moving the rod array away from the outlet capillary reduces the losses on the device outlet, but increases interface losses, so that total losses remain relatively constant.

Design Concept Screen 3

Using insight from the RE-c + RA-a case, the third design screening iteration introduces a forth RE geometry (RE-d), as illustrated by Fig. 2c. Here, the MP walls are initially twice as far away from the outlet capillary (maximum width of 36 mm) and gradually taper towards the original elliptical cross-section. The intention of this design concept is to keep the patient interface walls away from the flow when it is dispersed by the rod array to reduce device outlet and MP losses. The RE-d + RA-a case was evaluated as this rod array has provided good performance in the previous iterations and for direct comparison with the RE-a + RA-a case. RE-d + RA-e used the best-performing rod array from the second design screen iteration and tested whether the large number of rods was necessary to reduce interface losses despite the drawbacks in terms of MP construction. RE-d + RA-g is similar to RE-d + RA-e, but the rods span half the width of the patient interface, with this design included as an intermediate step. The RE-d + RA-a-434 case is the same as RE-d + RA-a with the rods placed in a 4-3-4 configuration (as opposed to 3-4-3) and was evaluated to determine whether this configuration provided performance improvements over the other design concepts. Finally, the RE-d + RA-c-EC design concept uses the rod array positioning seen in the RA-c case with an extended capillary (EC) that protrudes 6.5 mm into the patient interface. The intention of this design is to keep the inlet jet away from the device outlet and interface walls while forcing the flow through the rod array to disperse the jet and reduce its intensity.

Table III. Comparison of peak velocity (Peak Vel.), predicted regional deposition efficiencies (DE) in the device (Dev), mouthpiece (MP), and mouth-throat (MT), and predicted total deposition fraction (DF_{Tot}) among the original mouthpiece, the best cases from Design Screen 1, and Design Screen 2

Case	Peak Vel. [m/s]	DE_{Dev} [%]	DE_{MP} [%]	DE_{MT} [%]	DF_{Tot} [%]
Original MP	10.5	2.4	6.4	8.8	16.7
Design Screen 1 Best Cases					
RE-a	5.0	4.4	1.8	6.1	11.8
RA-a	2.7	27.7	7.7	4.9	36.5
Design Screen 2					
RE-a & RA-a[a]	2.1	6.0	4.9	4.6	**14.6**
RE-a & RA-c	2.6	1.9	13.2	4.9	19.0
RE-c & RA-a	3.9	22.5	10.6	5.5	34.5
CE & RA-a[a]	2.0	6.8	4.4	4.5	**14.9**
CE & RA-d	3.3	6.6	3.3	5.2	14.4
CE & RA-e[a]	1.8	1.9	7.4	4.4	**13.1**
CE & RA-f	1.7	0.8	9.5	4.4	14.1

RE Rapid Expansion, *RA* Rod Array, *CE* Cylindrical Expansion
[a] These cases demonstrated a marked improvement in predicted total deposition fraction over the rod array cases from Design Screen 1, when combined with the rapid expansion or cylindrical geometry, but further improvements are possible

The results in Table IV show all design concepts from the third screening iteration provided CFD-predicted total losses of less than 10% in the device outlet, patient interface, and MT regions. Widening the MP geometry had the expected effect of preventing the dispersed jet from depositing particles on the interface walls, which is clearly apparent when comparing the RE-d + RA-a case with RE-a + RA-a, as the wider geometry reduced total losses by 5.9% absolute difference. There was little difference in performance between the RE-d + RA-e and RE-d + RA-g cases, with the latter preferred as it required less rods and is hence easier to build. Switching the rod array configuration from 3-4-3 to 4-3-4 (RE-d + RA-a-434) gave a marginal improvement in reducing MP losses, but gave a higher peak jet velocity and therefore larger predicted MT losses, with total losses 0.9%

higher (absolute difference) compared to the original configuration. Finally, extending the outlet capillary into the MP (RE-d + RA-c-EC) provided the expected improvement of reducing device outlet losses, and had total depositional losses that are comparable with the other design concepts in the third iteration.

Figure 9 demonstrates the performance of the 3D rod array in diffusing the air-jet passing through the patient interface. Figure 9a shows the highly turbulent, high-velocity jet, which is generated by the DPI outlet capillary, entering the RE-a MP design candidate. This jet extends beyond the outlet of the patient interface and imparts a large amount of momentum on the aerosol, which leads to increased deposition on the first impaction point that the jet encounters, as described previously. The jet diffusion by the 3-4-3

Table IV. Comparison of peak velocity (Peak Vel.), predicted regional deposition efficiencies (DE) in the device (Dev), mouthpiece (MP), and mouth-throat (MT), and predicted total deposition fraction (DF_{Tot}) among the original mouthpiece, the best cases from Design Screens 1 and 2, and Design Screen 3

Case	Peak Vel. [m/s]	DE_{Dev} [%]	DE_{MP} [%]	DE_{MT} [%]	DF_{Tot} [%]
Original MP	10.5	2.4	6.4	8.8	16.7
Design Screen 1 and 2 Best Cases					
RE-a[b]	5.0	4.4	1.8	6.1	11.8
RE-a & RA-a	2.1	6.0	4.9	4.6	14.6
CE & RA-a	3.3	6.6	3.3	5.2	14.4
CE & RA-e	1.8	1.9	7.4	4.4	13.1
Design Screen 3					
RE-d & RA-a[a,b]	2.3	2.1	2.2	4.7	**8.7**
RE-d & RA-e[a]	2.4	0.6	2.0	4.8	**7.2**
RE-d & RA-g[a,b]	2.7	0.9	1.7	4.9	**7.4**
RE-d & RA-a-434	3.9	2.9	1.4	5.5	9.6
RE-d & RA-c-EC[a,b]	2.7	0.7	3.0	4.9	**8.4**

RE Rapid Expansion, *RA* Rod Array; CE Cylindrical Expansion, *434* 4-3-4 rod array configuration (as opposed to 3-4-3), *EC* Extended capillary from device outlet (inlet to MP)
[a] These cases demonstrate a dramatic improvement in predicted total deposition fraction (<9% combined MP and MT losses) compared to previous design screens
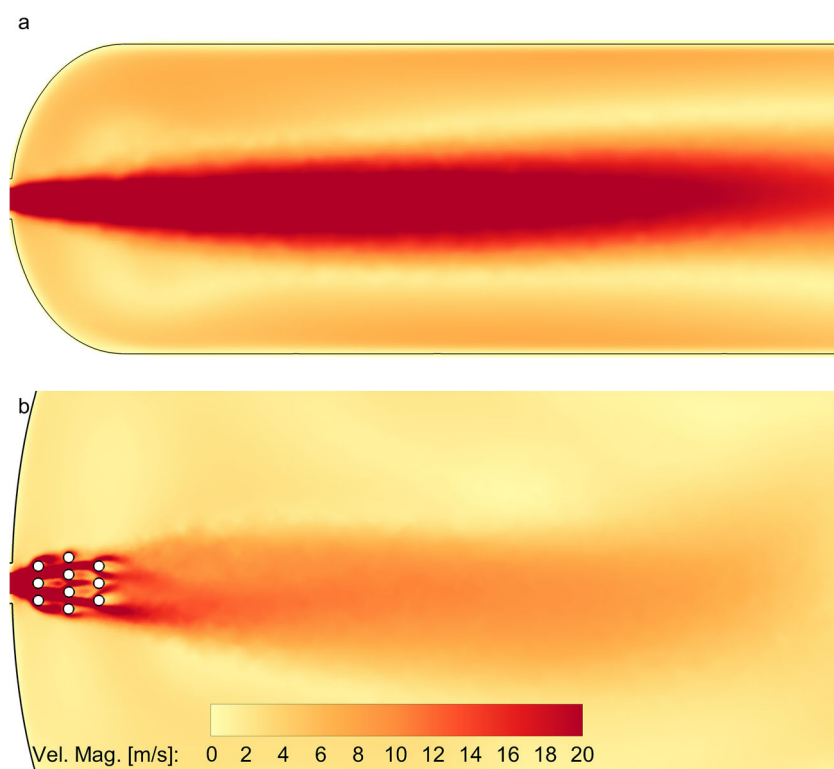[b] Candidate design concepts selected for evaluation with full mouthpiece and mouth-throat CFD model

Fig. 9. Example of jet diffusion by 3D rod array in the RE-d + RA-a mouthpiece compared to the high-velocity inlet jet in the RE-a design. Contours depict nodal values of velocity magnitude (Vel. Mag.) on an axial slice though the mid-plane of the patient interface

configuration rod array is clearly apparent in Fig. 9b, with the jet almost fully dissipated by approximately 30 mm into the 75 mm length of the RE-d + RA-a MP design. The vast reduction in peak velocity of the flow leaving the patient interface is expected to both reduce delivery system and ET losses, based on the previously presented deposition correlations.

Candidate Mouthpiece Designs

Four design concepts from the screening iterations were selected for evaluation with full MP and MT CFD models: RE-a, RE-d + RA-a, RE-d + RA-g, and RE-d + RA-a-EC. Figure 10 shows the CFD-predicted deposition patterns and regional DEs for the four candidate design concepts simulated in conjunction with the MT geometry. Only bin sizes from 1.09 to 3.26 μm are included in Fig. 10 as they account for 84% of the initial particle size distribution and provide a clearer representation of deposition patterns in the CFD domain. Comparing losses in Fig. 10b–d with Fig. 10a clearly shows that widening the MP geometry and including a rod array to disperse the inlet jet provides a substantial reduction in CFD-predicted patient interface and ET depositional losses, with an absolute difference in total DF of 10.3%. The best-performing case of the four candidate designs was RE-d + RA-a-EC with CFD-predicted total losses of 5.1% on the device outlet, MP, and MT region, which is a threefold reduction compared with the original MP (see Fig. 6a). Comparing regional deposition between RE-d + RA-a-EC and the original MP, CFD-predicted losses were reduced

from 2.4 to 0.6% on the device outlet, 6.4 to 2.2% on the MP, and 8.8 to 2.4% in the MT region.

Candidate Nasal Cannula Designs

The top four MP design concepts were applied to the NC flow pathway, which consists of the region between the outlet capillary and cannula bifurcation. Figure 11 shows the deposition patterns and regional DEs for the four NC designs. As with the MP flow pathway, widening the NC geometry and including a rod array (Fig. 11b–d) reduces total depositional losses compared to RE-a by a twofold reduction (Fig. 11a). Also consistent with the MP designs, the best-performing NC case was the RE-d + RA-a-EC design in Fig. 11d. Comparing the RE-d + RA-a-EC MP and NC directly, device outlet losses were similar (0.6% *vs.* 0.8%) and interface losses were a little higher in the NC with an absolute difference of 1.1%.

Optimal Flow Rate for Nasal Administration

The results in Fig. 11 are consistent with previous findings from this study that changes to the flow pathway in the NC, and the subsequent changes to the flow profile entering the nasal cavity have little effect on reducing NT losses. Figures 6d and 8c show that imposing a jet or turbulent velocity profile resulted in negligible difference in NT losses, and similarly, Fig. 11b–d show little change in NT losses despite the same design concepts reducing MT losses by 6.4% (absolute difference) when applied to the MP interface. One method to reduce impaction deposition in the NT region is to
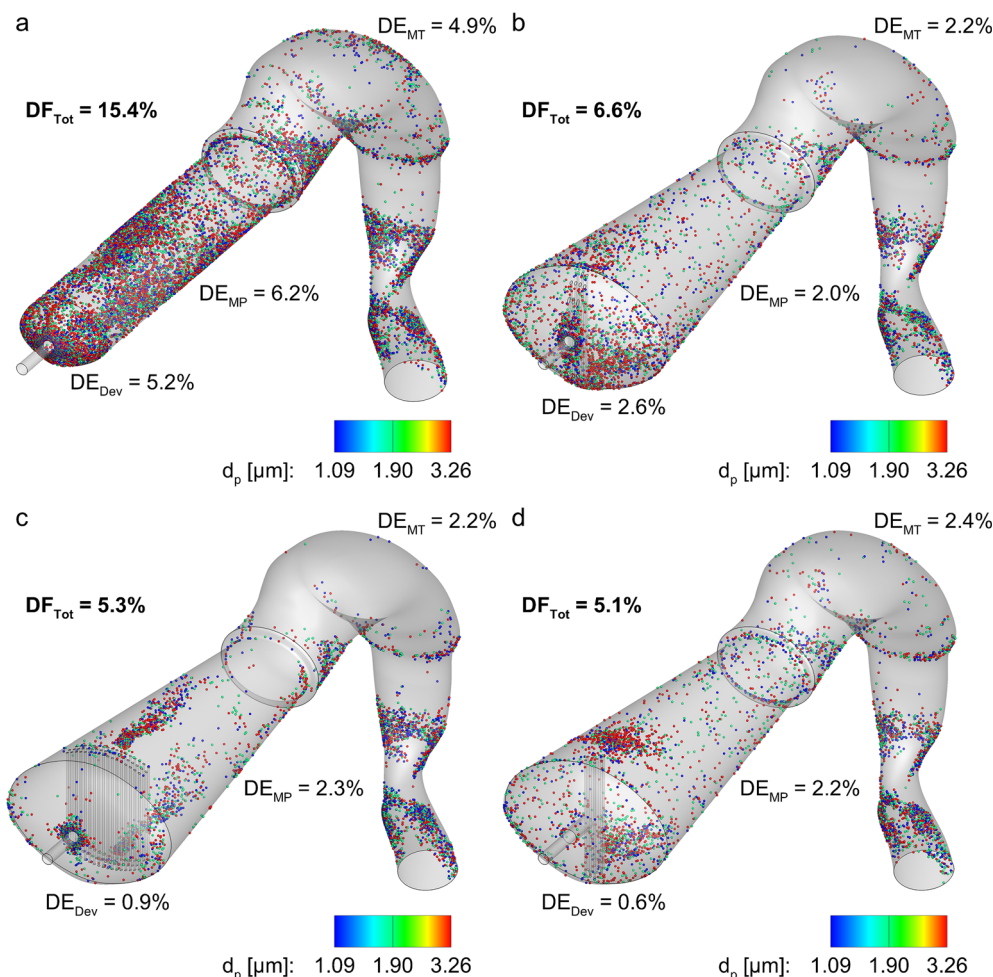
Fig. 10. Deposition patterns in full mouthpiece and mouth-throat model for the **a** RE-a, **b** RE-d + RA-a, **c** RE-d + RA-g, and **d** RE-d + RA-c-EC design concepts (see Fig. 7 for a description of the naming convention)

reduce the size of the aerosol that enters the nasal cavity, but exploratory work of this approach yielded little performance improvement as the 1.69-μm MMAD from the DPI is at the lower end of the characteristic S-curve deposition profile.

The alternative approach to reduce impaction deposition is to lower the flow rate through the patient interface and NT to reduce particle momentum. Figure 12 compares the CFD-predicted particle deposition for the best-performing NC design concept (RE-d + RA-c-EC) at the original operating flow rate (13.3 LPM) and 75% of that inlet flow rate (9.9 LPM; 25% reduction). The lower flow rate reduces NT losses by 6.9% (absolute difference) and total losses by 7.8%. The total interface and NT depositional loss at 9.9 LPM is 16.3%, which appears acceptably low.

DISCUSSION

This study met its objective by presenting three MP design concepts that provide CFD-predicted total depositional losses of less than 15%, with the best case being the RE-d + RA-a-EC design that showed a total DF on the device outlet, patient interface, and MT region of 5.1%. Combining these CFD-predicted interface and ET losses with the

approximate 10% device loss from Farkas et al. (6) suggests the possibility of a pediatric lung dose greater than 85% of the loaded dose. The NC design concepts did not perform as well as the MP designs with respect to increasing lung dose, as changes to the flow pathway had little effect on reducing NT losses. The combination of the RE-d + RA-a-EC design concept with a reduced operating flow rate of 9.9 LPM (25% decrease) gave a CFD-predicted total DF of 16.3%. Previous work showed that device losses are strongly associated with flow rate through the pediatric air-jet DPI (9); hence, operation of the delivery system at a lower flow rate, to reduce NT losses, may lead to increased device losses. However, experimental results of the device (Case 1.60/2.39) that had a 25% reduction in flow rate from the Bass et al. study (9) gave negligible change in MMAD (1.69 vs. 1.71 μm) and a 2.5% increase (absolute difference) in device losses. Therefore, overall system losses may be improved when administering the aerosol via N2L delivery at a reduced flow rate. Adding this loss to the experimentally determined DPI loss (6) suggests a lung dose that is approximately 74% of the loaded dose. This is slightly outside the performance targets laid out in the objective (lung dose > 75%), but the validation cases showed that the CFD models over-predict deposition in
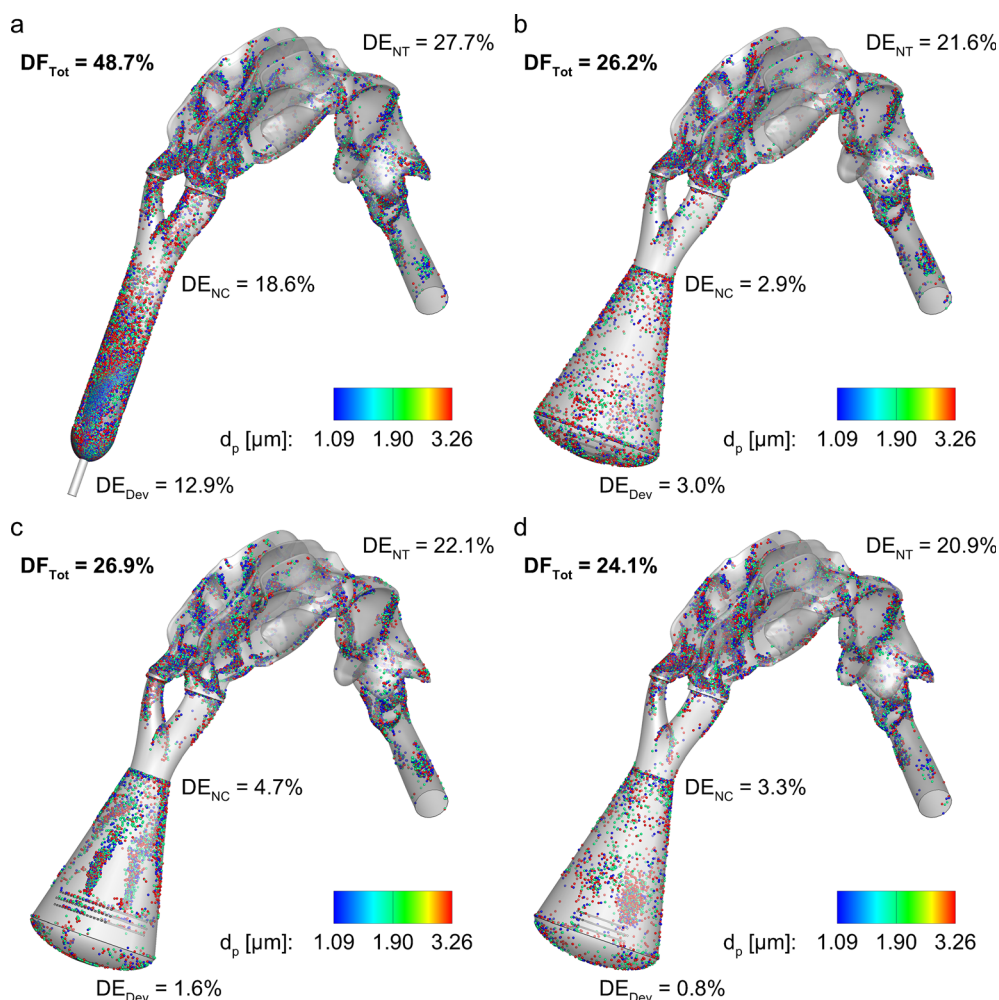
Fig. 11. Deposition patterns in full nasal cannula and nose-throat model for the **a** RE-a, **b** RE-d + RA-a, **c** RE-d + RA-g, and **d** RE-d + RA-c-EC design concepts (see Fig. 7 for a description of the naming convention)

the NC and NT, so there is a possibility that experimentally determined losses may be less than those suggested by these CFD predictions.

The CFD-predicted patient interface and ET losses, and associated lung dose, for these candidate design concepts must be experimentally tested, which will be the focus of a future study related to the development of this system for administration of tobramycin to pediatric patients with CF. The candidate design concepts also met the sizing and construction considerations that were stated in the objective. The total length to the MP and NC designs is less than 75 mm and no wider than 40 mm, which allows for a compact and portable device. The best-performing RE-d + RA-a-EC design concept also requires relatively few rods in the rod array, with a total of seven compared to other concepts that required more than 50, which allows for simplified construction of the patient interfaces. Considering volume, the MP and NC interfaces that employ the RE-d geometry had total internal volumes of 31 and 21 cm^3, respectively, which can easily be cleared with device actuation volumes on the order of 100 mL or more.

In addition to the primary objective, this study presents correlations that predict deposition in the MT and cannula bifurcation regions based on the maximum inlet velocity to each of these regions, with the same volumetric flow rate. The results show that imposing different velocity profiles with varying peak velocities can cause the CFD-predicted deposition to range from 3.8 to 8.8% in the MT region and from 0.9 to 7.2% in the cannula bifurcation. Using these predictive correlations reduced the turnaround time for analyzing numerous design candidates as only the flow pathway for each patient interface was required for each CFD model. The reduction in processing time using this method was especially important in this study as the oscillatory nature of the high-velocity inlet jet required a transient solution of the transport equations.

The deposition correlation results also show that the impaction deposition in the chosen region is dependent on the inlet velocity profile and not simply the inlet volumetric flow rate. Each of the four velocity profiles in Fig. 5a have the same flow rate, which was 13.3 LPM to be consistent with the chosen DPI, but each resulted in considerably different particle deposition results. A common method of predicting ET losses is to utilize the impaction parameter ($d_a^2 Q$) where particle size (d_a) and flow rate (Q) are used to estimate transmission through the MT or NT region (34–37). Studies
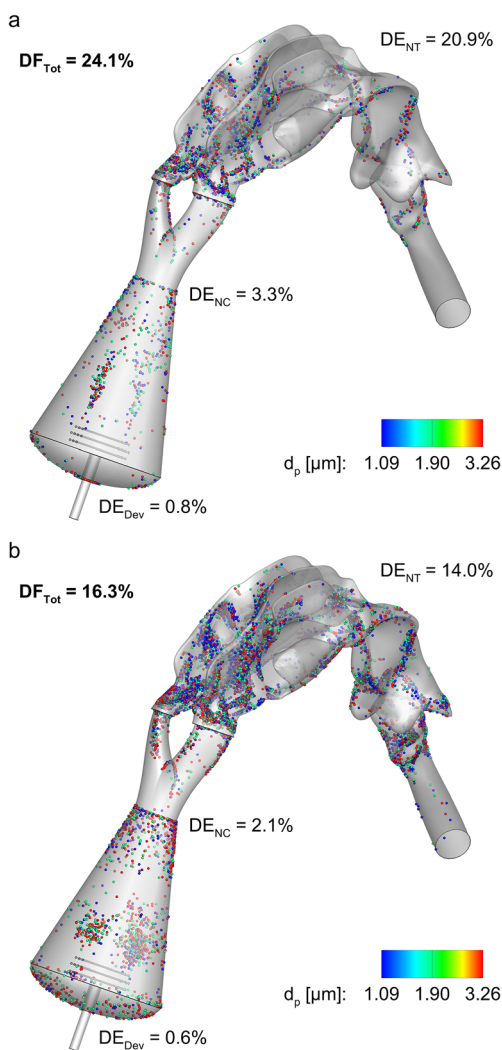
Fig. 12. Comparison of CFD-predicted deposition for the RE-d + RA-c-EC nasal cannula design operated at **a** 13.3 LPM and **b** 9.9 LPM (75%)

that use the impaction parameter typically describe a large amount of variability, with Golshahi et al. (34), Storey-Bishoff et al. (36), and Tavernini et al. (37) providing correlations that reduce this variability for children, infants, and neonates, respectively. The results in Fig. 8 show that for a constant flow rate, the deposition results increased substantially with respect to peak inlet velocity, which suggests that peak inlet velocity is also a significant indicator of ET deposition. As such, the variability in predicting ET losses with the impaction parameter may be reduced further if aspects of the inlet profile were taken into consideration. For example, operating conditions that result in a turbulent flow regime may have a lower peak velocity, due to the blunt turbulent velocity profile, which may result in lower deposition than even laminar flow if turbulent particle diperson is low. Similarly, if the flow does not reach a fully developed state before entering the experimental model, the inlet velocity could be very different from either a laminar (parabolic) or turbulent (blunt) profile, which could influence the development of extratoracic deposition correlations.

As mentioned previously, particle deposition was higher in the NT models compared to the MT, which resulted in lower expected lung doses with nasal administration. This apparent disadvantage of the NC designs can be leveraged as a benefit for the treatment of bacterial infections in the nasal cavity. There is evidence in the literature that the nasal cavity and sinuses can harbor bacterial colonies that repeatedly lead to lung infections in patients with CF (38–40) despite elimination of bacteria in the lower airways. Therefore, treatment methods may attempt to eradicate infections by administering tobramycin in the nasal cavity and sinuses. This would mean that nasal administration with the NC designs in the current study would be a preferred method, as a portion of the delivered dose is deposited in the NT region. If treatment of bacterial infections in the nasal cavity is not deemed necessary by clinicians and a high lung dose is required, then oral administration methods with the MP designs presented here would be the preferred method. Beyond discussions of targeting deposition in the various regions of the airways for uniform dosing, there are also practical aspects of oral and nasal administration that should be taken into consideration. The proposed system aims to deliver the lung inhalation volume to the subject during actuation, as well as the tobramycin dose, which requires an air-tight seal between the device and patient.

Limitations of this study primarily include the assumptions and approximations made by the CFD models. Hygroscopic growth is known to increase particle size as the aerosol travels through the humid airways. This phenomenon was neglected from the CFD model as the increase in ET deposition from hygroscopic growth is expected to be small, with Walenga et al. (41) reporting an approximate 0.1% increase in adult nasal airways. The same negligible impact on ET deposition in infant and pediatric airways can also be assumed in the present study. The rod array was added to the patient interface in an effort to diffuse the high-velocity inlet jet, but rod arrays have also previously been utilized to increase secondary particle breakup and reduce aerosol size (15–18). This secondary breakup mechanism was not included in the CFD models due to the associated increase in complexity and processing times. The deaggregation from passing the aerosol through the rod array decreases the particle size, which would be expected to decrease interface and ET losses and lead to further improvements in lung dose. These potential improvements to the delivery system performance that were not captured by the CFD models will be experimentally tested in a subsequent study. The disadvantage of including a rod array in the patient interface design is that placing obstacles in the flow would lead to an increase in impaction deposition. However, the CFD models assumed the stainless-steel rods did not trap any particles that contact the surface (*i.e.*, a reflection boundary condition was applied). Our previous work with rod arrays has shown the losses on the stainless-steel cylindrical surfaces are small and matched *in vitro* validation data (17,18), but this assumption must also be tested experimentally.

CONCLUSION

In conclusion, candidate MP design concepts were developed that provide total CFD-predicted losses of approximately 5%, and expected lung doses of approximately 85% (when coupled with the best-case DPI from Farkas et al. (6)). Candidate NC design concepts performed slightly worse than their MP counterparts, but operating the DPI with a 25% reduction in flow rate led to an expected lung delivery efficiency of approximately 74%. Development of deposition correlations showed that losses were strongly related to peak velocity on the outlet plane of the interface flow pathway, while the flow rate through the device was maintained at 13.3 LPM. Findings from this study and our previous publications on the subject will be used in the continuing development of a tobramycin delivery system for treating CF lung infections in pediatric patients.

ACKNOWLEDGMENTS

Disclaimer   The content is solely the responsibility of the authors and does not necessarily represent the official views of the National Institutes of Health.

FUNDING INFORMATION

COMPLIANCE WITH ETHICAL STANDARDS

Conflict of Interest Virginia Commonwealth University is currently pursuing patent protection of EEG aerosol delivery, DPI aerosol generation devices and patient interfaces, which if licensed, may provide a future financial interest to the authors.

REFERENCES

1. Somayaji R, Parkins MD. Tobramycin inhalation powder: an efficient and efficacious therapy for the treatment of Pseudomonas aeruginosa infection in cystic fibrosis. Ther Deliv. 2015;6(2):121–37.
2. Below A, Bickmann D, Breitkreutz J. Assessing the performance of two dry powder inhalers in preschool children using an idealized pediatric upper airway model. Int J Pharm. 2013;444(1–2):169–74.
3. Lindert S, Below A, Breitkreutz J. Performance of dry powder inhalers with single dosed capsules in preschool children and adults using improved upper airway models. Pharmaceutics. 2014;6:36–51.
4. Lexmond AJ, Hagedoorn P, Frijlink HW, Rottier BL, de Boer AH. Prerequisites for a dry powder inhaler for children with cystic fibrosis. PLoS One. 2017;12(8):e0183130.
5. Lexmond AJ, Kruizinga TJ, Hagedoorn P, Rottier BL, Frijlink HW, De Boer AH. Effect of inhaler design variables on paediatric use of dry powder inhalers. PLoS One. 2014;9(6):e99304.
6. Farkas D, Hindle M, Bass K, Longest PW. Development of an inline dry powder inhaler for oral or trans-nasal aerosol administration to children. J Aerosol Med Pulm Drug Deliv. 2019.
7. Longest PW, Farkas D. Development of a new inhaler for high-efficiency dispersion of spray-dried powders using computational fluid dynamics (CFD) modeling. AAPS J. 2018. https://doi.org/10.1208/s12248-018-0281-y.
8. Longest PW, Farkas D, Bass K, Hindle M. Use of computational fluid dynamics (CFD) dispersion parameters in the development of a new DPI actuated with low air volumes. Pharm Res. 2019;36(8).
9. Bass K, Farkas D, Longest PW. Optimizing aerosolization using computational fluid dynamics in a pediatric air-jet dry powder inhaler. AAPS PharmSciTech. 2019;20(8).
10. Hindle M, Longest PW. Quantitative analysis and design of a spray aerosol inhaler. Part 2: improvements in mouthpiece performance. J Aerosol Med Pulm Drug Deliv. 2013;26(5):237–47.
11. Farkas D, Hindle M, Longest PW. Application of an inline dry powder inhaler to deliver high dose pharmaceutical aerosols during low flow nasal cannula therapy. Int J Pharm. 2018;546(1–2):1–9.
12. Farkas D, Hindle M, Longest PW. Efficient nose-to-lung aerosol delivery with an inline dpi requiring low actuation air volume. Pharm Res. 2018;35(10).
13. Coates MS, Chan H-K, Fletcher DF, Chiou H. Influence of mouthpiece geometry on the aerosol delivery performance of a dry powder inhalation. Pharm Res. 2007;24(8):1450–6.
14. Coates MS, Fletcher DF, Chan H-K, Raper JA. Effect of design on the performance of a dry powder inhaler using computational fluid dynamics. Part 1: grid structure and mouthpiece length. J Pharm Sci-Us. 2004;93(11):2863–76.
15. Behara SRB, Longest PW, Farkas DR, Hindle M. Development of high efficiency ventilation bag actuated dry powder inhalers. Int J Pharm. 2014;465(1–2):52–62.
16. Behara SRB, Longest PW, Farkas DR, Hindle M. Development and comparison of new high-efficiency dry powder inhalers for carrier-free formulations. J Pharm Sci-US. 2014;103(2):465–77.
17. Longest PW, Golshahi L, Behara SRB, Tian G, Farkas DR, Hindle M. Efficient nose-to-lung (N2L) aerosol delivery with a dry powder inhaler. J Aerosol Med Pulm Drug Deliv. 2015;28(3):189–201.
18. Longest PW, Son Y-J, Holbrook LT, Hindle M. Aerodynamic factors responsible for the deaggregation of carrier-free drug powders to form micrometer and submicrometer aerosols. Pharm Res. 2013;30:1608–27.
19. Bass K, Boc S, Hindle M, Dodson K, Longest PW. High-efficiency nose-to-lung aerosol delivery in an infant: development of a validated computational fluid dynamics method. J Aerosol Med Pulm Drug Deliv. 2019. https://doi.org/10.1089/jamp.2018.1490.
20. Bass K, Longest PW. Recommendations for simulating microparticle deposition at conditions similar to the upper airways with two-equation turbulence models. J Aerosol Sci. 2018.
21. Longest PW, Vinchurkar S. Validating CFD predictions of respiratory aerosol deposition: effects of upstream transition and turbulence. J Biomech. 2007;40(2):305–16.
22. Delvadia R, Longest PW, Byron PR. In vitro tests for aerosol deposition. I. Scaling a physical model of the upper airways to predict drug deposition variation in normal humans. J Aerosol Med. 2012;25(1):32–40.

23. Wei X, Hindle M, Kaviratna A, Huynh BK, Delvadia RR, Sandell D, et al. In vitro tests for aerosol deposition. VI: realistic testing with different mouth–throat models and in vitro—in vivo correlations for a dry powder inhaler, metered dose inhaler, and soft mist inhaler. J Aerosol Med Pulm Drug Deliv. 2018.

24. Roache PJ. Perspective: a method for uniform reporting of grid refinement studies. J Fluid Eng Trans ASME. 1994;116(3):405–13.

25. Longest PW, Hindle M, Das Choudhuri S, Byron PR. Numerical simulations of capillary aerosol generation: CFD model development and comparisons with experimental data. Aerosol Sci Technol. 2007;41(10):952–73.

26. Longest PW, Vinchurkar S, Martonen TB. Transport and deposition of respiratory aerosols in models of childhood asthma. J Aerosol Sci. 2006;37:1234–57.

27. Longest PW, Xi J. Effectiveness of direct Lagrangian tracking models for simulating nanoparticle deposition in the upper airways. Aerosol Sci Technol. 2007;41(4):380–97.

28. Walenga RL, Longest PW. Current inhalers deliver very small doses to the lower tracheobronchial airways: assessment of healthy and constricted lungs. J Pharm Sci. 2016;105:147–59.

29. Matida EA, Finlay WH, Grgic LB. Improved numerical simulation of aerosol deposition in an idealized mouth-throat. J Aerosol Sci. 2004;35:1–19.

30. Wang Y, James PW. On the effect of anisotropy on the turbulent dispersion and deposition of small particles. Int J Multiphase Flow. 1999;22:551–8.

31. Tian G, Hindle M, Lee S, Longest PW. Validating CFD predictions of pharmaceutical aerosol deposition with in vivo data. Pharm Res. 2015;32:3170–87.

32. White FM. Viscous fluid flow. 3rd ed. New York: McGraw-Hill Higher Education; 2006. xxi, 629 pages p

33. Longest PW, Vinchurkar S. Effects of mesh style and grid convergence on particle deposition in bifurcating airway models with comparisons to experimental data. Med Eng Phys. 2007;29(3):350–66.

34. Golshahi L, Noga ML, Thompson RB, Finlay WH. In vitro deposition measurement of inhaled micrometer-sized particle in extrathoracic airways of children and adolescents during nose breathing. J Aerosol Sci. 2011;42:474–88.

35. Javaheri E, Golshahi L, Finlay W. An idealized geometry that mimics average infant nasal airway deposition. J Aerosol Sci. 2013;55:137–48.

36. Storey-Bishoff J, Noga M, Finlay WH. Deposition of micrometer-sized aerosol particles in infant nasal airway replicas. Aerosol Sci. 2008;39:1055–65.

37. Tavernini S, Church TK, Lewis DA, Noga M, Martin AR, Finlay WH. Deposition of micrometer-sized aerosol particles in neonatal nasal airway replicas. Aerosol Sci Technol. 2018;52(4):407–19.

38. Hansen SK, Rau MH, Johansen HK, Ciofu O, Jelsbak L, Yang L, et al. Evolution and diversification of Pseudomonas aeruginosa in the paranasal sinuses of cystic fibrosis children have implications for chronic lung infection. ISME J. 2012;6(1):31–45.

39. Linnane B, Kearse L, O'Connell NH, Fenton J, Kiernan MG, Dunne CP. A case of failed eradication of cystic fibrosis-related sinus colonisation by Pseudomonas aeruginosa. BMC Pulm Med. 2015;15.

40. Moller ME, Alanin MC, Gronhoj C, Aanaes K, Hoiby N, von Buchwald C. Sinus bacteriology in patients with cystic fibrosis or primary ciliary dyskinesia: a systematic review. Am J Rhinol Allergy. 2017;31(5):293–8.

41. Walenga RL, Tian G, Hindle M, Yelverton J, Dodson K, Longest PW. Variability in nose-to-lung aerosol delivery. J Aerosol Sci. 2014;78:11–29.